ภาคผนวก

Ghost modes and continuum scattering in the dimerized distorted kagome lattice antiferromagnet $Rb_2Cu_3SnF_{12}$

K. Matan,[1,2,*] Y. Nambu,[3] Y. Zhao,[4,5] T. J. Sato,[3] Y. Fukumoto,[6] T. Ono,[7] H. Tanaka,[8,†] C. Broholm,[5,9,10] A. Podlesnyak,[10] and G. Ehlers[10]

[1]*Department of Physics, Faculty of Science, Mahidol University, Bangkok 10400, Thailand*
[2]*ThEP, Commission of Higher Education, Bangkok 10400, Thailand*
[3]*IMRAM, Tohoku University, Sendai, Miyagi 980-8577, Japan*
[4]*Department of Materials Science and Engineering, University of Maryland, College Park, Maryland 20742, USA*
[5]*NIST Center for Neutron Research, National Institute of Standards and Technology, Gaithersburg, Maryland 20899, USA*
[6]*Department of Physics, Faculty of Science and Technology, Tokyo University of Science, Noda, Chiba 278-8510, Japan*
[7]*Department of Physical Science, School of Science, Osaka Prefecture University, Sakai, Osaka 599-8531, Japan*
[8]*Department of Physics, Tokyo Institute of Technology, Meguro-ku, Tokyo 152-8551, Japan*
[9]*Institute for Quantum Matter and Department of Physics and Astronomy, The Johns Hopkins University, Baltimore, Maryland 21218, USA*
[10]*Quantum Condensed Matter Division, Oak Ridge National Laboratory, Oak Ridge, Tennessee 37831, USA*

(Received 17 May 2013; revised manuscript received 27 December 2013; published 21 January 2014)

High-intensity pulsed neutron scattering reveals a new set of magnetic excitations in the pinwheel valence-bond solid state of the distorted kagome lattice antiferromagnet $Rb_2Cu_3SnF_{12}$. The polarization of the dominant dispersive modes (2 meV $< \hbar\omega <$ 7 meV) is determined and found consistent with a dimer series expansion with strong Dzyaloshinskii–Moriya interactions ($D/J = 0.18$). A weakly dispersive mode near 5 meV and shifted "ghosts" of the main modes are attributed to the enlarged unit cell below a $T = 215$ K structural transition. Continuum scattering between 8 and 10 meV might be interpreted as a remnant of the kagome spinon continuum [Nature (London) **492**, 406 (2012).].

DOI: 10.1103/PhysRevB.89.024414 PACS number(s): 75.10.Kt, 75.10.Jm, 78.70.Nx

I. INTRODUCTION

Interacting spins on the two-dimensional kagome lattice have fascinated physicists since Syozi first showed that Ising spins on this lattice, which he named after the woven pattern on a Japanese bamboo basket, do not order for $T \to 0$ [1]. More recently, efforts have focused on determining the ground state of the quantum spin-$\frac{1}{2}$ Heisenberg kagome lattice antiferromagnet, which is considered to be one of the most challenging problems in condensed matter physics. The complexity arises from the macroscopic degeneracy caused by the incompatibility between the global geometry of the corner-sharing triangular network and local, nearest-neighbor antiferromagnetic interactions [2]. The classical Néel state is apparently replaced by a dynamic quantum state, the details of which remain to be established. Proposed ground states include a gapless U(1)-Dirac-spin-liquid state [3–6], a gapped-spin-liquid [7–11], and valence-bond-solid (VBS) states [12–16]. These states are very close in energy so small perturbations and intrinsic limitations of numerical methods make it difficult to reach a firm conclusion. Most of the recent theoretical studies point to a quantum spin liquid [17] although there is no consensus on its precise nature.

Identifying an ideal kagome lattice model system has also proven to be difficult. All realizations so far have been plagued by magnetic impurities, lattice distortion, and extra terms in the spin Hamiltonian including anisotropic and further-neighbor interactions [18–28]. Albeit minuscule in some cases, these effects may conceal the intrinsic nature of the nearest-neighbor Heisenberg kagome antiferromagnet (HKAFM). Still, much can be learned by studying materials with interacting quantum spins on kagome-like lattices. For the quantum spin-$\frac{1}{2}$ kagome lattice antiferromagnet $ZnCu_3(OH)_6Cl_2$ (herbertsmithite), a recent experiment by Han *et al.* indicates that fractionalized excitations, a key characteristic of spin liquids, are robust against a small excess of Cu^{2+} ions in the interlayer sites and against anisotropic Dzyaloshinskii–Moriya (DM) interactions [29]. The recent discovery of the pinwheel VBS state in the distorted kagome lattice antiferromagnet $Rb_2Cu_3SnF_{12}$ offers a rare opportunity to study a cooperative singlet on an approximate kagome lattice [30]. Besides being unique and interesting in its own right, the pinwheel VBS state may display intersite correlations and excitations related to the ideal HKAFM [31].

At room temperature, $Rb_2Cu_3SnF_{12}$ has the hexagonal $R\bar{3}$ space group with lattice parameters $a = 13.917(2)$ Å and $c = 20.356(3)$ Å [32]. At 215 K, it undergoes a first-order structural transition, doubling the in-plane lattice constant a. The resulting lattice distortion is small [30] so to a first approximation we use the room-temperature structure, where a two-dimensional unit cell comprises 12 Cu^{2+} spins [Fig. 1(a)]. The spin-$\frac{1}{2}$ Cu^{2+} ions form a distorted kagome plane and are surrounded by a deformed octahedral environment of fluorine. The kagome planes are separated by nonmagnetic ions, which results in weak interlayer interactions. The distorted kagome lattice gives rise to four antiferromagnetic in-plane exchange interactions $J_1 > J_2 > J_3 > J_4$ [Fig. 1(a)]. To lowest order, spins interacting through J_1 form singlets which are linked through the weaker interactions. Powder neutron diffraction shows no magnetic order down to 1.3 K. The low-temperature magnetic susceptibility indicates a nonmagnetic, spin singlet ($S_{tot} = 0$) ground state and mixing of the singlet and triplet

*kittiwit.mat@mahidol.ac.th
†tanaka@lee.phys.titech.ac.jp

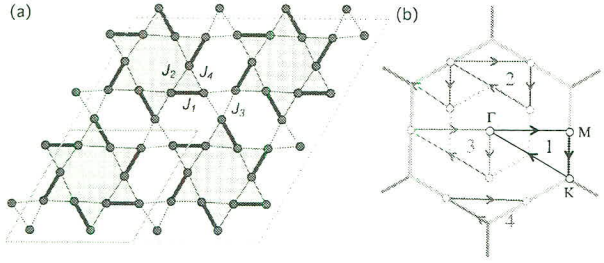

FIG. 1. (Color online) (a) The pinwheel VBS state is formed by dimers (thick lines). A dimer is a pair of spins with the largest exchange interaction J_1. The exchange interactions are $J_1 > J_2 > J_3 > J_4$. Yellow solid lines denote a two-dimensional unit cell of the room-temperature phase while yellow dotted lines denote the $2a \times 2a$ enlarged unit cell. (b) A diagram showing paths 1, 2, 3, and 4 in the first Brillouin zone. The dotted hexagon denotes the smaller Brillouin zone associated with the enlarged unit cell.

($S_{\rm tot} = 1$) excited states through the DM interactions [33] ($S_{\rm tot}$ denotes the quantum number for the total spin of a single dimer). To a good approximation, the spin Hamiltonian is given by

$$\mathcal{H} = \sum_{nn} \left[J_{ij} \mathbf{S}_i \cdot \mathbf{S}_j + \mathbf{D}_{ij} \cdot \mathbf{S}_i \times \mathbf{S}_j \right], \qquad (1)$$

where $J_{ij} > 0$ are the nearest-neighbor antiferromagnetic exchange interactions, and $\mathbf{D}_{ij}$ are the corresponding DM vectors.

In a previous study [30] involving several of the present authors, magnetic excitations from the singlet ground state were probed using inelastic neutron scattering on a triple-axis spectrometer. These measurements revealed the pinwheel motif of dimers and determined the relevant spin Hamiltonian parameters through a dimer series expansion up to eighth order. However, the detailed structure of the excitations could not be resolved due to lack of resolution and counting statistics (see Fig. 2 in Ref. [30]). Here we report high-intensity pulsed neutron scattering measurements on single crystalline $Rb_2Cu_3SnF_{12}$ using the Cold Neutron Chopper Spectrometer at the Spallation Neutron Source, Oak Ridge National Laboratory [34]. A time-resolved, highly pixelated detector system that covers a large solid angle (14% of the unit sphere) enabled concurrent measurements over a much wider range of momentum and at higher resolution than previously. We confirm the splitting of the triplet associated with dimerization into a doublet and a singlet as a result of strongly anisotropic interactions and are able to unambiguously determine the polarization of each mode. More importantly, we discover a new family of modes associated with the structural superlattice, and a continuum at high energy, which may be related to the spinon continuum recently detected in the undimerized kagome system, herbertsmithite [29].

The article is organized as follows: In Sec. II, we describe the inelastic neutron scattering experiment and the resulting data. In Sec. III A, the measured magnetic excitations are analyzed in the framework of a dimer series expansion for the $2a \times 2a$ enlarged unit cell. We find very good agreement for energy transfer less than 8 meV. We analyze the wave-vector dependence of scattering perpendicular to the kagome planes to determine the magnetic polarization of each mode in Sec. III B. This confirms that the triplet is split into a singlet and a doublet. Section III C is devoted to a discussion of the excitation spectrum and continuum scattering between 8 and 10 meV, which cannot be explained by the dimer series expansion. We end with a summary in Sec. IV.

II. EXPERIMENT AND RESULTS

Single-crystalline $Rb_2Cu_3SnF_{12}$ was synthesized from the melt using the method described in Ref. [33]. Inelastic neutron scattering measurements were performed on two co-aligned crystals with a total mass of 4 g and a mosaic of 1.5°. The sample was mounted with the $(H,0,L)$ reciprocal lattice plane horizontal to allow intensity integration of rod-like scattering along the L direction while taking advantage of the two dimensionality of the system. The incident energy E_i was fixed at 12 meV for an energy resolution (full width at half maximum) of 0.56(3) meV at the elastic position. The sample was cooled to a base temperature of 2 K using a He-4 cryostat. Multiple datasets were acquired by rotating the sample about the vertical axis, which is parallel to $[-1,2,0]$, in steps of 2° covering 68° of sample orientation. An angle between the incident beam and $[0,0,1]$ ranges from −28.5° to 39.5°. The background was measured at 70 K, where the excitations are very broad and weak [30]. These datasets were subsequently combined to produce a background-subtracted, four-dimensional scattering-intensity function $I(\mathbf{Q},\hbar\omega)$, where $\mathbf{Q}$ is the momentum transfer and $\hbar\omega$ is the energy transfer. The data were sliced and cut along high-symmetry directions using MSLICE [35] to produce contour maps and constant-$\mathbf{Q}$ and constant-energy plots.

A contour map of $\hbar\omega \cdot I(\mathbf{Q},\hbar\omega)$ averaged over the L direction (the L dependence of the scattering intensity will be discussed later), which is plotted as a function of energy and in-plane momentum along $[H,0]$ [Fig. 2(a)], shows a distinct pattern of excitations around $(-2,0)$ and faint outlines of similar patterns displaced by $\Delta H = \pm 4$. The latter are barely detectable around the equivalent Brillouin-zone centers, $(-6,0)$ and $(2,0)$. The measurements were set up so integration along L is optimal at $(-2,0)$. The difference in the intensity profile around $(-2,0)$ and $(2,0)$ is a result of a smaller range of intensity integration for the latter. The overall profile of the excitations around $(-2,0)$ is consistent with our previous report [30]. The lower branch, which has a broader bandwidth, is known to be a twofold-degenerate excitation as it is split by a magnetic field along the c direction [30]. By mapping the L dependence of the intensity of this branch, we shall later show that it is associated with transitions from the singlet ground state ($S_{\rm tot} = 0$) to a doublet with $S_{\rm tot} = 1$ and $S_{{\rm tot},z} = \pm 1$ ($S_{{\rm tot},z}$ denotes the magnetic quantum number of the $S_{\rm tot} = 1$ triplet states). The upper branch, which has a smaller bandwidth, does not split in a field and so is thought to be a nondegenerate excitation from the singlet ground state to the singlet state with $S_{\rm tot} = 1$ and $S_{{\rm tot},z} = 0$. We note that these states are not pure states of defined angular momentum due to the DM interactions.

A constant-$\mathbf{Q}$ cut at $(-2,0)$ [Fig. 2(d)] shows clear resolution-limited peaks at $\hbar\omega = 2.4(3)$ and 6.9(3) meV, consistent with the previous data (where the uncertainty represents half the energy resolution). The contour maps around the zone

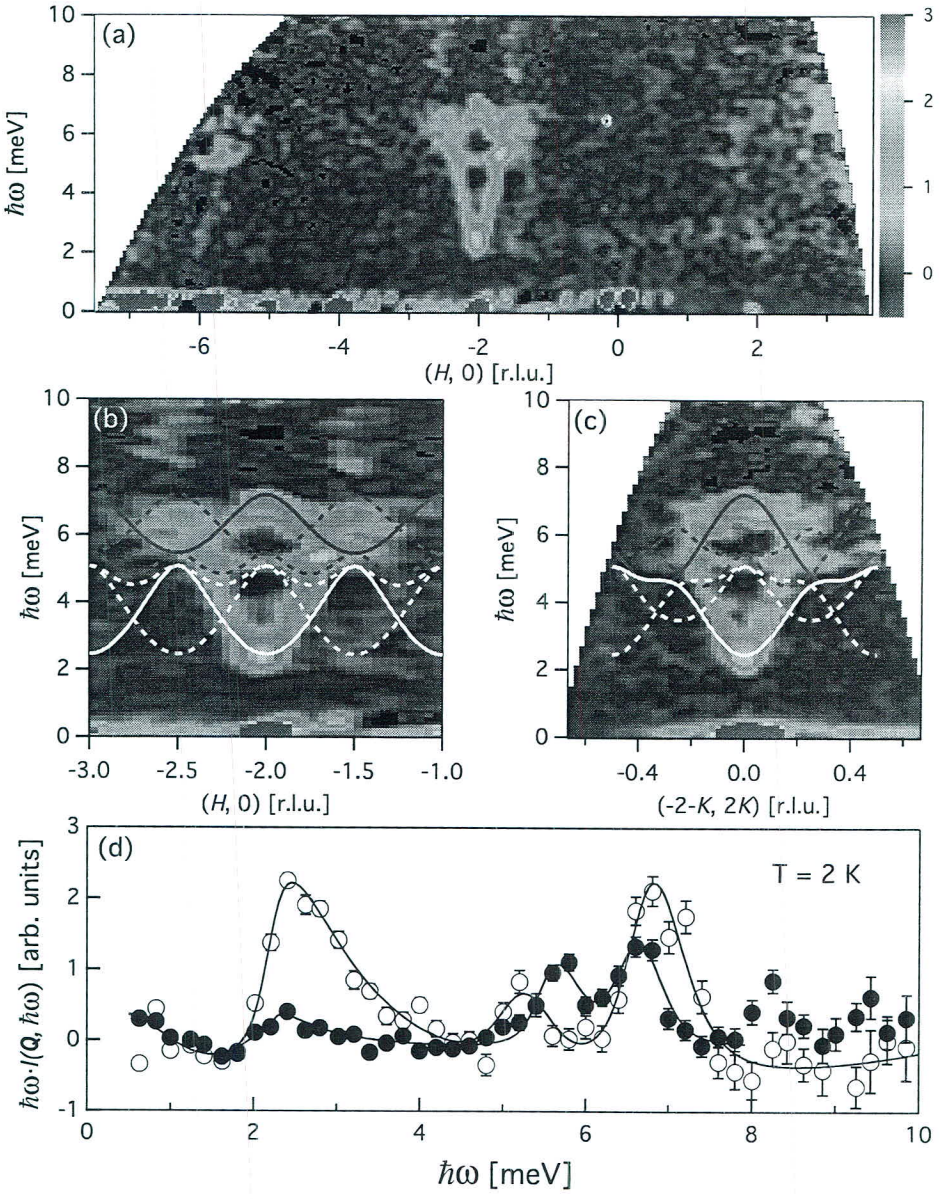

FIG. 2. (Color online) Contour maps show a product of scattering intensity and energy transfer $\hbar\omega \cdot I(\mathbf{Q},\hbar\omega)$, displaying magnetic excitations in $Rb_2Cu_3SnF_{12}$ as a function of energy and in-plane momentum through (a), (b) $(H,0)$ and (c) $(-2-K,2K)$. The intensity is averaged over the available range of L, $\Delta\mathbf{Q}_{[1,0]}$ of 0.042 Å^{-1}, and $\Delta\mathbf{Q}_{[-1,2]}$ of 0.045 Å^{-1}. The measurements along $[-K,2K]$ are limited by a smaller detector-coverage area perpendicular to the horizontal plane. Solid lines represent the excitations of the original spin Hamiltonian whereas dotted lines denote excitations resulting from the $2a \times 2a$ enlarged unit cell. Red denotes the $S_{\mathrm{tot},z} = 0$ mode and white denotes the $S_{\mathrm{tot},z} = \pm 1$ mode. (d) Constant-$\mathbf{Q}$ cuts show $\hbar\omega \cdot I(\mathbf{Q},\hbar\omega)$ at $(-2,0)$ (open circles) and the average of $\hbar\omega \cdot I(\mathbf{Q},\hbar\omega)$ at $(-1.5,0)$ and $(-2.5,0)$ (closed circles). Above 8 meV, the closed symbols lie above background, indicative of the continuum scattering. The lines are guides to the eye. The error bar represents one standard deviation.

center $(-2,0)$ [Figs. 2(b) and 2(c)] reveal a more intricate set of excitations than previously appreciated. A weakly dispersive mode around 5 meV is visible along both $[H,0]$ and $[-K,2K]$ [Figs. 2(b) and 2(c)]. At the zone center this mode peaks at 5.3(3) meV [Fig. 2(d)]. It grows slightly more intense away from the zone center, which contrasts with the other two modes that become weaker. We also observe excitations centered around $(-1.5,0)$ and $(-2.5,0)$ [Figs. 2(b) and 5(a) (2.0 to 2.5 meV)], which resemble the mode around $(-2,0)$, but with much less intensity, and hence are named the "ghost" modes. We have previously reported these ghost modes and attributed them to the enlarged unit cell caused by the structural transition [30]. Our dimer series expansion shown by solid lines in Figs. 2(b) and 2(c) and the bond-operator mean-field theory

[36] cannot account for all of this observed scattering intensity between 2 and 7 meV as neither calculation considers the enlarged unit cell. Furthermore, we observe diffuse scattering between 8 and 10 meV near (−1.5,0) and (−2.5,0), which cannot be accounted for by the dimer series expansion.

III. ANALYSIS AND DISCUSSION

In this section, we first analyze the excitation dispersions below 8 meV using the extended version of the dimer series expansion, which has been discussed in our previous work [30], to include the effect of the enlarged unit cell. We then investigate the L dependence of the intensity to determine the polarization of each mode. We end this section with a discussion of the diffuse scattering between 8 and 10 meV.

A. Dimer series expansion and enlarged unit cell

To understand the 5 meV mode and the ghost modes around (−1.5,0) and (−2.5,0), we consider the $2a \times 2a$ enlarged unit cell consisting of 48 spins shown in Fig. 1(a). We write the spin Hamiltonian as $\mathcal{H} + H'$, where $\mathcal{H}'$ represents a perturbation due to the enlarged unit cell. $\mathcal{H}'$ has the exact same form as $\mathcal{H}$ [Eq. (1)] but the sum is over 48 spins in the enlarged unit cell [see Fig. 1(a)]. We then perform the dimer series expansion on the pinwheel VBS state using the Hamiltonian $\mathcal{H} + H'$. The linked cluster expansion algorithm was used to generate a graphical series of dimers [37]. The low-energy spectra are calculated up to eighth order in the interdimer and DM interactions using the Dlog–Padé approximation [30]. We define the path $\Gamma \rightarrow M \rightarrow K \rightarrow \Gamma$ in the first Brillouin zone of the original model $\mathcal{H}$ as path 1 [Fig. 1(b)]. The lowest-energy excitations with $S_{\mathrm{tot},z} = \pm 1$ and those with $S_{\mathrm{tot},z} = 0$ along path 1 are shown in Fig. 3(a). We also define paths 2, 3, and 4 [Fig. 1(b)], which differ by a reciprocal lattice vector of the enlarged unit cell. Dispersion curves for paths 2, 3, and 4 are shown in Figs. 3(b), 3(c), and 3(d), respectively. In Figs. 2(b) and 2(c) path 1 shown as solid lines and paths 2, 3, and 4 shown as dotted lines are qualitatively in agreement with the data. If $\mathcal{H}'$ is nonzero but very small, then paths 2, 3, and 4 become equivalent to path 1, and the dispersion curves shown by dotted lines are the anticipated ghost modes together with the corresponding excitations of the original Hamiltonian.

It is interesting to note that the weakly dispersive mode in Fig. 2(b) is originally the excitation on the path between two adjacent M points [paths 2 and 4 in Fig. 1(b)]. From the experiment, this mode is not symmetric around $H = -1.75$; its energy increases monotonically as H varies from −2 to −1.5. This suggests that we observe the $S_{\mathrm{tot},z} = \pm 1$ triplet excitations around the zone center, $H = -2$, and the $S_{\mathrm{tot},z} = 0$ triplet excitations away from there, which may be experimentally verified by measurements in a magnetic field. We note that the in-plane component of the DM vector d_p is set to zero in our dimer series expansion. A recent ^{63,65}Cu NMR study in high fields up to 30 T [38] and neutron scattering measurements [39] show that the mixing between the singlet and triplet states via the DM interactions gives rise to a large residual gap. The anticrossing of the singlet and triplet mode, which is due to the combined effect of the off-diagonal g tensor and small d_p ($|d_p| < 0.012$) [38], prevents the gap from closing at high magnetic fields. However, d_p has little effect on the overall zero-field spectrum [30].

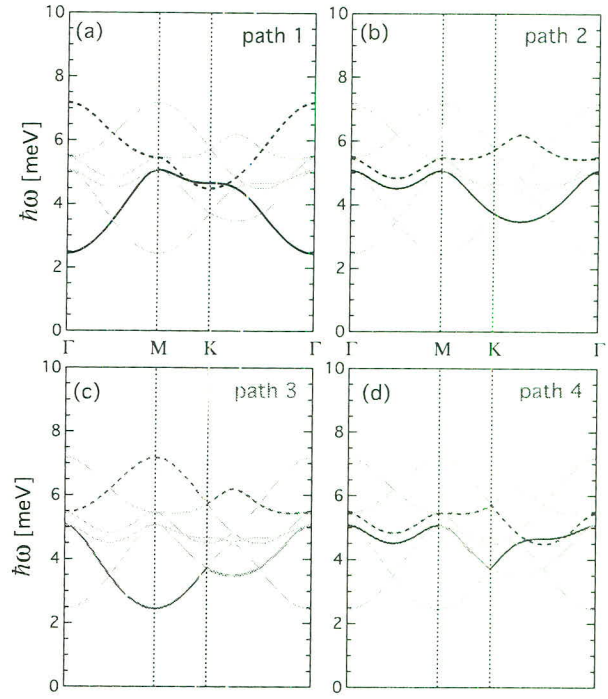

FIG. 3. (Color online) (a) Singlet-to-triplet excitations along path 1 [Fig. 1(b)] for the unperturbed Hamiltonian $\mathcal{H}$ are shown by black lines. Gray lines denote the modes resulting from the perturbed Hamiltonian $\mathcal{H}'$ associated with the enlarged unit cell. Solid lines denote excitations from the singlet ground state to the $S_{\mathrm{tot},z} = \pm 1$ states whereas dotted lines denote excitations to the the $S_{\mathrm{tot},z} = 0$ state. Colored solid and dotted lines in panels (b), (c), and (d) show the excitations along paths 2, 3, and 4 [Fig. 1(b)], respectively.

B. L dependence and mode polarization

The scattering intensity displayed thus far was averaged over the L direction. However, the L dependence of the scattering intensity contains valuable information about the polarization of the excitations and interplane correlations. Within the resolution of our measurements, there is no dispersion along L [Fig. 4(a)], which attests to the two-dimensional nature of the system. Contour maps of the scattering intensity integrated over the energy ranges $\hbar\omega =$ [2.0,3.0] meV [Fig. 4(b)] and $\hbar\omega =$ [6.5,7.5] meV [Fig. 4(c)] plotted as a function of H and L show rods of scattering that extend along L at $H = -6$, −2, and 2. The integrated intensity of the $S_{\mathrm{tot},z} = \pm 1$ mode has broad maxima at $L = 3$ and 6 before falling off at large L [Fig. 4(d)], while that of the $S_{\mathrm{tot},z} = 0$ mode monotonically decreases as a function of L with a small hump around $L = 6$ [Fig. 4(e)]. The overall trend of the curves reflects the different polarization of the modes while the modulation of scattering intensity results from interplane correlations. The magnetic scattering cross section

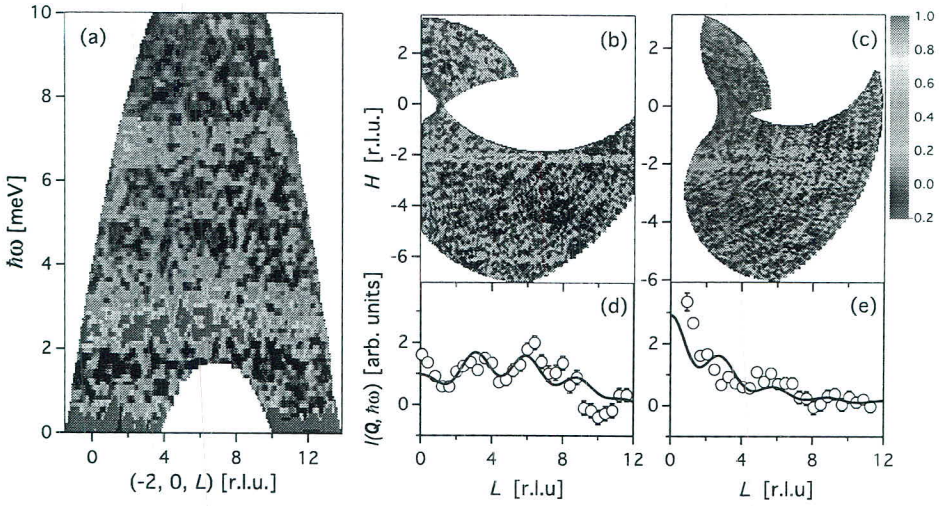

FIG. 4. (Color online) (a) Contour maps of $I(\mathbf{Q},\hbar\omega)$ are plotted as a function of $\hbar\omega$ and L. The intensity is averaged over $\Delta\mathbf{Q}_{[1,0]}$ of 0.042 Å^{-1} and $\Delta\mathbf{Q}_{[-1,2]}$ of 0.045 Å^{-1}. The broadening is a result of the integration along the in-plane momenta. Panels (b) and (c) show contour maps of $I(\mathbf{Q},\hbar\omega)$ plotted as a function of H and L. The intensity is energy integrated for (b) $\hbar\omega = [2.0,3.0]$ meV and (c) $\hbar\omega = [6.5,7.5]$ meV. Panels (d) and (e) show the L dependence of $I(\mathbf{Q},\hbar\omega)$ for energy ranges (d) $\hbar\omega = [1.0,4.0]$ meV and (e) $\hbar\omega = [6.0,8.0]$ meV centered at $(-2,0)$. The intensity is averaged over $\Delta\mathbf{Q}_{[1,0]}$ of 0.10 Å^{-1} and $\Delta\mathbf{Q}_{[-1,2]}$ of 0.18 Å^{-1}. Solid lines denote the product of the magnetic form factor for Cu^{2+} spins, the interplane correlation function, and the polarization factor, assuming that modes are polarized (d) in the kagome plane and (e) out of the plane.

[40] can be described by

$$\frac{d^2\sigma}{d\Omega dE'} = N_M \frac{\mathbf{k}'}{\mathbf{k}}(\gamma r_0)^2 \left[\frac{g}{2} f(\mathbf{Q}) e^{-W}\right]^2 \times \sum_{\alpha,\beta}(\delta_{\alpha\beta} - \hat{Q}_\alpha \hat{Q}_\beta) S^{\alpha\beta}(\mathbf{Q},\omega), \qquad (2)$$

where the $\mathbf{Q}$-dependent terms are the magnetic form factor $f(\mathbf{Q})$ and the dynamic magnetic structure factor $S^{\alpha\beta}(\mathbf{Q},\omega)$, which is the space and time Fourier transform of the spin-pair correlation function. The magnetic scattering cross section also contains the polarization factor that arises from the anisotropy of the dipole-dipole interaction between neutrons and electrons.

For the magnetic excitations in $Rb_2Cu_3SnF_{12}$, the polarization factor becomes $1 \underset{(-)}{+} (Q_L/|\mathbf{Q}|)^2$, where Q_L is a component of $\mathbf{Q}$ along L. It grows (shrinks) with increasing L if the polarization is in plane or transverse (out of plane or longitudinal) [40]. The interplane correlations, which are embedded in the dynamic structure factor, can be described by a function $1 + \alpha\cos(\frac{2\pi L}{3})$, when the correlations along c only extend to the nearest-neighbor plane located at $\frac{c}{3}$. Here the fit parameter α indicates the type and strength of interplane correlations. (Ferromagnetic for positive α, antiferromagnetic for negative α.) The product of the magnetic form factor for Cu^{2+} spins, which decreases monotonically with increasing L, the polarization factor, and the interplane correlation function denoted by a solid line in Fig. 4(d) [Fig. 4(e)] is in accordance with the in-plane (out-of-plane) polarization of the $S_{\text{tot},z} = \pm 1$ ($S_{\text{tot},z} = 0$) mode. Ferromagnetic interplane correlations are indicated by positive α [$\alpha = 0.31(15)$]. The polarization analysis for the excitations around 5 meV close to the zone boundary, which is not shown, reveals mixing of the in-plane and out-of plane polarizations, or in other words the $S_{\text{tot},z} = 0$ and $S_{\text{tot},z} = \pm 1$ modes merge near the zone boundary.

C. Continuum scattering

The magnetic excitation spectrum between 2 and 7 meV in $Rb_2Cu_3SnF_{12}$ is markedly different from the spin-wave excitations observed in the classical spin-$\frac{5}{2}$ kagome lattice antiferromagnet $KFe_3(OH)_6(SO_4)_2$ (jarosite), which orders magnetically at low temperatures [41]. It also differs from the continuum of spinon excitations in herbertsmithite, where the ground state is believed to be a quantum spin liquid [29]. Resonant modes in $Rb_2Cu_3SnF_{12}$ [Fig. 5(a)] are found only around the zone center and their intensity decreases precipitously away from $(-2,0)$, while in jarosite the "weathervane" mode exists throughout the Brillouin zone and in herbertsmithite the spinon continuum gives rise to hexagonal rings of diffuse scattering, surrounding zone centers [29]. However, between 8 and 10 meV we observe for $Rb_2Cu_3SnF_{12}$ weak diffuse scattering near $(-1.5,0)$ and $(-2.5,0)$ [Figs. 2(b), 2(d), and 5(b)] on both sides of the zone center $(-2,0)$, as in herbertsmithite. This scattering, which is diffuse in energy and broad in momentum, is different from the resolution-limited excitations below 8 meV and cannot be accounted for within the dimer series expansion. For herbertsmithite, the recent neutron scattering places an upper bound of 0.25 meV on any gap in the continuum of scattering [29]. On the contrary, the continuum in $Rb_2Cu_3SnF_{12}$ is observed well above the sharp dispersive modes of the pinwheel VBS state. Thus, while pinwheel dimerization and DM interactions in $Rb_2Cu_3SnF_{12}$ induce resonant modes at low energies, it appears that a threshold in energy exists beyond which a spin flip is no longer

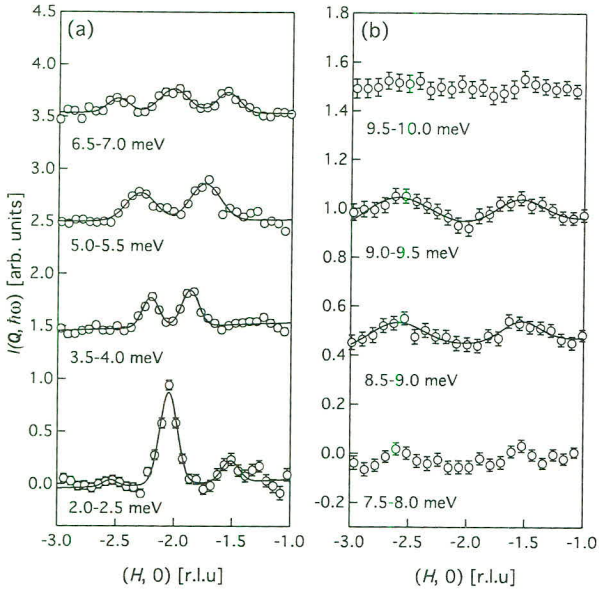

FIG. 5. Constant-energy cuts of $I(\mathbf{Q},\hbar\omega)$ are plotted as a function of H. The energy range of the integration is indicated below each data set. The intensity is averaged over the whole range of L and $\Delta\mathbf{Q}_{[-1,2]}$ of 0.045 Å^{-1}. The lines serve as guides to the eye. Data sets for different energy ranges in panels (a) and (b) are shifted vertically by 1 (1.5 for 2.0 to 2.5 meV) and 0.5, respectively.

a stable quasiparticle and the underlying quantum kagome nature of the material is apparent. Whether this scattering is best interpreted as resulting from two-magnon processes or magnon fractionalization will require a more detailed comparison between theories incorporating such features [42] and higher-quality scattering data.

IV. SUMMARY

High-intensity high-resolution pulsed neutron scattering unveils new features of the magnetic excitations in the pinwheel VBS state of the distorted kagome lattice antiferromagnet $Rb_2Cu_3SnF_{12}$. We observe a weakly dispersive mode around 5 meV and ghost modes, both of which are attributed to the enlarged unit cell caused by the structural transition at $T = 215$ K. Excitations below 8 meV appear to be well described by the dimer series expansion for the enlarged unit cell. The polarization analysis of the dominant modes is consistent with a splitting of the triplet into a $S_{\mathrm{tot},z} = 0$ singlet and a $S_{\mathrm{tot},z} = \pm 1$ doublet due to DM interactions. Between 8 and 10 meV, we observe continuum scattering, which is reminiscent of the fractionalized excitations recently observed in herbertsmithite.

ACKNOWLEDGMENTS

The work was supported in part by the Thailand Research Fund under Grant No. MRG55800, a Grant-in-Aid for Scientific Research from JPS (Grants No. 23244072, No. 24740223, and No. 23540395) and a Global COE Program funded by MEXT Japan. Work at the Institute for Quantum Matter was supported by the US Department of Energy, Office of Basic Energy Sciences, Division of Materials Sciences and Engineering under Award DE-FG02-08ER46544. The research at Oak Ridge National Laboratory's Spallation Neutron Source was sponsored by the Scientific User Facilities Division, Office of Basic Energy Sciences, U.S. Department of Energy.

[1] I. Syozi, Prog. Theor. Phys. **6**, 306 (1951).
[2] A. P. Ramirez, *Handbook of Magnetic Materials*, edited by K. H. J. Buschow (Elsevier Science, Amsterdam, 2001), Vol. 13, pp. 423–520.
[3] M. B. Hastings, Phys. Rev. B **63**, 014413 (2000).
[4] Y. Ran, M. Hermele, P. A. Lee, and X.-G. Wen, Phys. Rev. Lett. **98**, 117205 (2007).
[5] Y. Iqbal, F. Becca, S. Sorella, and D. Poilblanc, Phys. Rev. B **87**, 060405 (2013).
[6] Y. Iqbal, F. Becca, and D. Poilblanc, New J. Phys. **14**, 115031 (2012).
[7] S. Sachdev, Phys. Rev. B **45**, 12377 (1992).
[8] C. Waldtmann, H. U. Everts, B. Bernu, C. Lhuillier, P. Sindzingre, P. Lecheminant, and L. Pierre, Eur. Phys. J. B **2**, 501 (1998).
[9] C. Zeng and V. Elser, Phys. Rev. B **51**, 8318 (1995).
[10] G. Misguich, D. Serban, and V. Pasquier, Phys. Rev. Lett. **89**, 137202 (2002).
[11] S. Depenbrock, I. P. McCulloch, and U. Schollwöck, Phys. Rev. Lett. **109**, 067201 (2012).
[12] J. B. Marston and C. Zeng, J. Appl. Phys. **69**, 5962 (1991).
[13] P. Nikolic and T. Senthil, Phys. Rev. B **68**, 214415 (2003).
[14] R. R. P. Singh and D. A. Huse, Phys. Rev. B **76**, 180407(R) (2007).
[15] R. R. P. Singh and D. A. Huse, Phys. Rev. B **77**, 144415 (2008).
[16] B.-J. Yang, Y. B. Kim, J. Yu, and K. Park, Phys. Rev. B **77**, 224424 (2008).
[17] S. Yan, D. A. Huse, and S. R. White, Science **332**, 1173 (2011).
[18] J. S. Helton, K. Matan, M. P. Shores, E. A. Nytko, B. M. Bartlett, Y. Yoshida, Y. Takano, A. Suslov, Y. Qiu, J. H. Chung *et al.*, Phys. Rev. Lett. **98**, 107204 (2007).
[19] J. S. Helton, K. Matan, M. P. Shores, E. A. Nytko, B. M. Bartlett, Y. Qiu, D. G. Nocera, and Y. S. Lee, Phys. Rev. Lett. **104**, 147201 (2010).
[20] S.-H. Lee, H. Kikuchi, Y. Qiu, B. Lake, Q. Huang, K. Habicht, and K. Kiefer, Nat. Mater. **6**, 853 (2007).
[21] T.-H. Han, S. Chu, and Y. S. Lee, Phys. Rev. Lett. **108**, 157202 (2012).
[22] T.-H. Han, J. S. Helton, S. Chu, A. Prodi, D. K. Singh, C. Mazzoli, P. Muller, D. G. Nocera, and Y. S. Lee, Phys. Rev. B **83**, 100402 (2011).
[23] O. Ofer and A. Keren, Phys. Rev. B **79**, 134424 (2009).

[24] P. Mendels, F. Bert, M. A. deVries, A. Olariu, A. Harrison, F. Duc, J. C. Trombe, J. S. Lord, A. Amato, and C. Baines, Phys. Rev. Lett. **98**, 077204 (2007).
[25] F. Bert, D. Bono, P. Mendels, F. Ladieu, F. Duc, J. C. Trombe, and P. Millet, Phys. Rev. Lett. **95**, 087203 (2005).
[26] H. Yoshida, Y. Okamoto, T. Tayama, T. Sakakibara, M. Tokunaga, A. Matsuo, Y. Narumi, K. Kindo, M. Yoshida, M. Takigawa *et al.*, J. Phys. Soc. Jpn. **78**, 043704 (2009).
[27] G. J. Nilsen, F. C. Coomer, M. A. de Vries, J. R. Stewart, P. P. Deen, A. Harrison, and H. M. Rønnow, Phys. Rev. B **84**, 172401 (2011).
[28] B. Fåk, E. Kermarrec, L. Messio, B. Bernu, C. Lhuillier, F. Bert, P. Mendels, B. Koteswararao, F. Bouquet, J. Ollivier *et al.*, Phys. Rev. Lett. **109**, 037208 (2012).
[29] T.-H. Han, J. S. Helton, S. Chu, D. G. Nocera, J. A. Rodriguez-Rivera, C. Broholm, and Y. S. Lee, Nature (London) **492**, 406 (2012).
[30] K. Matan, T. Ono, Y. Fukumoto, T. J. Sato, J. Yamaura, M. Yano, K. Morita, and H. Tanaka, Nat. Phys. **6**, 865 (2010).
[31] E. Khatami, R. R. P. Singh, and M. Rigol, Phys. Rev. B **84**, 224411 (2011).
[32] T. Ono, K. Morita, M. Yano, H. Tanaka, K. Fujii, H. Uekusa, Y. Narumi, and K. Kindo, Phys. Rev. B **79**, 174407 (2009).
[33] K. Morita, M. Yano, T. Ono, H. Tanaka, K. Fujii, H. Uekusa, Y. Narumi, and K. Kindo, J. Phys. Soc. Jpn. **77**, 043707 (2008).
[34] G. Ehlers, A. A. Podlesnyak, J. L. Niedziela, E. B. Iverson, and P. E. Sokol, Rev. Sci. Instrum. **82**, 085108 (2011).
[35] R. T. Azuah, L. R. Kneller, Y. Qiu, P. L. W. Tregenna-Piggott, C. M. Brown, and J. R. D. Copley, J. Res. Natl. Inst. Stand. Technol. **114**, 341 (2009).
[36] K. Hwang, K. Park, and Y. B. Kim, Phys. Rev. B **86**, 214407 (2012).
[37] J. Oitmaa, C. Hamer, and W. Zhang, *Series Expansion Methods for Strongly Interacting Lattice Models* (Cambridge University Press, Cambridge, 2006).
[38] M. S. Grbić, S. Krämer, C. Berthier, F. Trousselet, O. Cepas, H. Tanaka, and M. Horvatic, Phys. Rev. Lett. **110**, 247203 (2013).
[39] Y. Nambu *et al.* (unpublished).
[40] S. W. Lovesey, *Theory of Neutron Scattering From Condensed Matter, Volume 2: Polarization Effects and Magnetic Scattering* (Clarendon Press, Oxford, 1984).
[41] K. Matan, D. Grohol, D. G. Nocera, T. Yildirim, A. B. Harris, S.-H. Lee, S. E. Nagler, and Y. S. Lee, Phys. Rev. Lett. **96**, 247201 (2006).
[42] M. Mourigal, W. T. Fuhrman, A. L. Chernyshev, and M. E. Zhitomirsky, Phys. Rev. B **88**, 094407 (2013).

Journal of the Physical Society of Japan **83**, 043701 (2014)
http://dx.doi.org/10.7566/JPSJ.83.043701

Large Negative Quantum Renormalization of Excitation Energies in the Spin-1/2 Kagome Lattice Antiferromagnet $Cs_2Cu_3SnF_{12}$

Toshio Ono[1], Kittiwit Matan[2,3], Yusuke Nambu[4], Taku J. Sato[4], Kazuya Katayama[5], Satoshi Hirata[5], and Hidekazu Tanaka[5]

[1]*Department of Physical Science, School of Science, Osaka Prefecture University, Sakai 599-8531, Japan*
[2]*Department of Physics, Faculty of Science, Mahidol University, Bangkok 10400, Thailand*
[3]*ThEP, Commission of Higher Education, Bangkok 10400, Thailand*
[4]*Institute of Multidisciplinary Research for Advanced Materials, Tohoku University, Sendai 980-8577, Japan*
[5]*Department of Physics, Tokyo Institute of Technology, Meguro, Tokyo 152-8551, Japan*

(Received November 19, 2013; accepted February 14, 2014; published online March 5, 2014)

Magnetic excitations in the spin-1/2 distorted kagome lattice antiferromagnet $Cs_2Cu_3SnF_{12}$, which has an ordered ground state owing to the strong Dzyaloshinskii–Moriya interaction, were studied using inelastic neutron scattering. Although the spin-wave dispersion can be qualitatively understood in terms of linear spin-wave theory (LSWT), the excitation energies are renormalized by a factor of approximately 0.6 from those calculated by LSWT, almost irrespective of the momentum transfer. This inadequacy of LSWT, which is attributed to quantum fluctuations, provides evidence of negative quantum renormalization in the spin-1/2 kagome lattice antiferromagnet.

Ubiquitous magnetic excitations in conventional magnets with the Néel state are generally well described by LSWT. In low-dimensional quantum magnets, however, dominant quantum effects significantly modify the magnetic excitations. In particular, for an $S = 1/2$ antiferromagnetic Heisenberg spin chain, the exact spinon excitation energies are larger than that calculated using LSWT by a factor of $\pi/2$,[1] which was verified through an inelastic neutron scattering experiment on the spin-1/2 one-dimensional (1D) Heisenberg antiferromagnet $CuCl_2{\cdot}2N(C_5D_5)$.[2] This quantum enhancement of excitation energies is known as the quantum renormalization.

The spin-1/2 2D kagome-lattice antiferromagnet (KLAF) is a research frontier with the potential to realize a disordered ground state arising from the synergistic effect of strong frustration and quantum fluctuations.[3–13] The theoretical consensus for the case of Heisenberg spins is that the classical Néel state, which is robust in conventional magnets, is supplanted by a disordered quantum state. However, the nature of the ground state, which is the basis for the discussion of excitations, has not been theoretically elucidated. Innovative theoretical studies have been conducted on the spin-1/2 nearest-neighbor Heisenberg KLAF using a variety of approaches. Most of the recent results suggest the existence of nonmagnetic ground states described by spin liquids[6–10] and valence-bond solids.[11–13] Experimentally, the lack of an ideal model has hindered detailed studies of intrinsic excitations of kagome magnets. Nevertheless, great effort has been made to search for approximate realizations of the spin-1/2 KLAF, which exhibits a diversity of states.[14–22]

$A_2Cu_3SnF_{12}$ (A = Rb, Cs) is a promising family of spin-1/2 KLAFs.[20,21] $Rb_2Cu_3SnF_{12}$ has a distorted kagome lattice and a gapped $S = 0$ singlet ground state.[20–22] A study of singlet-to-triplet excitations in $Rb_2Cu_3SnF_{12}$ using inelastic neutron scattering revealed a pinwheel motif of strongly interacting dimers.[21–23] All relevant spin Hamiltonian parameters were determined, which suggested the dominant effect of the Dzyaloshinskii–Moriya (DM) interaction.[21–24] On the other hand, $Cs_2Cu_3SnF_{12}$ has a uniform kagome lattice at room temperature with the lattice parameters $a = 7.142(4)$ Å and $c = 20.381(14)$ Å,[20] as shown in Fig. 1(a). This compound undergoes a structural transition at $T_s = 185$ K and magnetic ordering at $T_N = 20.0$ K.[20] The magnetic susceptibility exhibits a small anomaly at T_s and a large increase at T_N [Fig. 2(a)]. The presence of superlattice reflections below T_s suggests the doubling of the in-plane lattice parameter, giving rise to a $2a \times 2a$ enlarged unit cell. Above T_N, the magnetic susceptibility is in good agreement with the theoretical susceptibility obtained from exact diagonalization for the 24-site kagome cluster[25] [Fig. 2(a)]. This suggests that the exchange network remains approximately uniform.

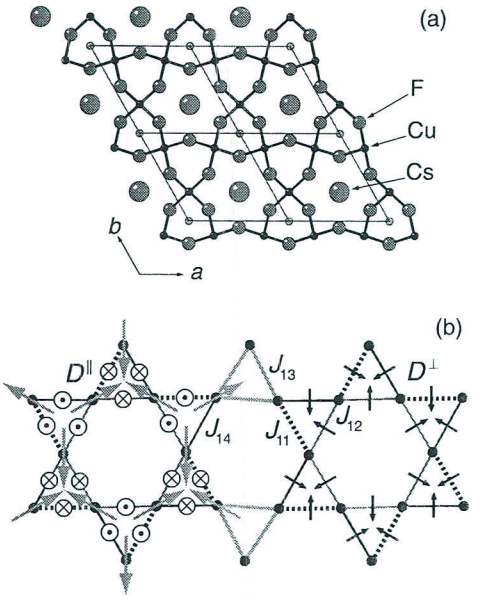

Fig. 1. (Color online) (a) Crystal structure at room temperature viewed along the *c*-axis, where fluorine ions located outside the kagome layer are omitted. Thin lines denote the unit cell. (b) Diagram showing the connectivity of $S = 1/2$ Cu^{2+} spins via the nearest-neighbor exchange interactions J_{11}, J_{12}, J_{13}, and J_{14}. Configurations of the out-of-plane component $D^{\parallel}$ and in-plane component $D^{\perp}$ of the DM vectors, deduced from the highly symmetric room-temperature structure, are illustrated on the left and right, respectively. The large arrows on the left indicate the $q = 0$ structure assumed in the LSWT calculations.

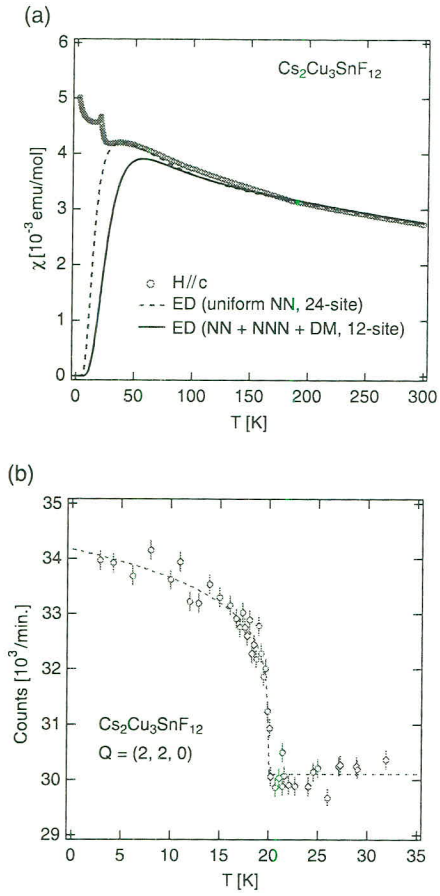

Fig. 2. (Color online) (a) Temperature dependence of magnetic susceptibility in $Cs_2Cu_3SnF_{12}$. Dashed line denotes the result obtained by exact diagonalization for a 24-site uniform kagome cluster with $J = 20.7$ meV and $g = 2.49$, while solid line is the result obtained for a 12-site distorted kagome cluster with $J_{avg} = 19.8$ meV and the same interaction coefficients a_i, J_2/J_1 and d_z as those obtained from the analysis of spin-wave dispersions with $d_p = 0$ and $g = 2.43$. (b) Temperature dependence of the magnetic Bragg reflection at $\boldsymbol{Q} = (2, 2, 0)$. The dashed line serves as a visual guide.

Low-energy magnetic excitations in the spin-1/2 distorted KLAF $Cs_2Cu_3SnF_{12}$ can be described by the collective disturbance of the ordered moments. Although these magnetic excitations in the classical spin-5/2 KLAF $KFe_3(OH)_6(SO_4)_2$ are well described by LSWT,[26,27] little is known about the quantum effect for the spin-1/2 case, where large quantum renormalization is expected to emerge. In this letter, we present the first evidence of the large negative renormalization of spin-wave energies with respect to the LSWT result in $Cs_2Cu_3SnF_{12}$. This observation provides a striking contrast to the well-known positive quantum renormalization of excitation energies in the $S = 1/2$ antiferromagnetic Heisenberg spin chain,[1] for which the renormalization factor is exactly $\pi/2$.

$Cs_2Cu_3SnF_{12}$ crystals were synthesized in accordance with the chemical reaction $2CsF + 3CuF_2 + SnF_4 \rightarrow Cs_2Cu_3SnF_{12}$. CsF, CuF_2, and SnF_4 were dehydrated by heating in vacuum at about 100 °C. First the materials were packed into a Pt tube of 9.6 mm inner diameter and 100 mm length in the ratio of 3 : 3 : 2. One end of the Pt tube was welded and the other end was tightly folded with pliers and placed between Nichrome plates. Single crystals were grown from the melt. The temperature of the furnace was lowered from 850 to 750 °C over 100 h. After collecting the well-formed pieces of crystal, we repeated the same procedure. Inelastic neutron scattering measurements were performed on two co-aligned single crystals of $Cs_2Cu_3SnF_{12}$ (total mass of 3.3 g) with a sample mosaic of about 1° at GPTAS and HER, which are triple-axis spectrometers run by the Institute for Solid State Physics, University of Tokyo. At GPTAS, the final energy of the thermal neutrons was fixed at 14.7 meV. The collimations were 40′–40′–sample–40′–80′. A pyrolytic graphite (PG) filter was placed after the sample to remove contamination from higher-order neutrons. The vertically focused (horizontally flat) PG crystals were used to analyze the scattered neutrons. At HER, the final energy of the cold neutrons was fixed at 5 meV. The scattered neutrons were analyzed using the central three blades of a seven-blade doubly focused PG analyzer. A cool Be or oriented-PG-crystal filter was placed in the incident beam and a room-temperature Be filter was placed in the scattered beam. In the analysis of the HER data, effective collimations of 10′–40′–sample–160′–120′ were used. For both experiments, the sample was aligned with the $(h, k, 0)$ plane horizontal to measure spin-wave excitations within the kagome plane. The sample was cooled to the base temperature of 3 K using a ^{4}He closed cycle cryostat.

Using the $2a \times 2a$ enlarged unit cell for the low-temperature crystal structure, we observed an increased scattering intensity due to magnetic Bragg reflections below $T_N = 20.0$ K at $\boldsymbol{Q}_m = (2m, 2n, 0)$, where m and n are integers. The ordering wave vectors correspond to the reciprocal lattice points of the uniform kagome lattice above $T_s = 185$ K. Figure 2(b) shows the temperature dependence of the magnetic Bragg reflection at $\boldsymbol{Q} = (2, 2, 0)$. The scattering intensity above $T_N = 20.0$ K arises from a nuclear reflection. This result indicates that the ordered state has a $\boldsymbol{q} = 0$ structure. Hence the center of the 2D Brillouin zone located at $\boldsymbol{Q}_m$ is expected to give rise to strong spin-wave scattering.

Figure 3(a) shows constant-$\boldsymbol{Q}$ scans measured using the GPTAS spectrometer. The scans were performed at 3 K and at three different momentum transfers $\boldsymbol{Q} = (2, 2, 0)$, $(2.25, 2, 0)$, and $(2.267, 1.867, 0)$. At the zone center (Γ-point) $\boldsymbol{Q} = (2, 2, 0)$, we clearly observed two spin-wave excitations at 10.7(5) and 13.6(4) meV, and extra scattering above the background below 5 meV [top panel of Fig. 3(a)]. A high-resolution measurement using the cold-neutron spectrometer HER revealed a spin gap of 1.0(6) meV as shown in Fig. 3(c). Away from the zone center along the Γ → M and Γ → K directions, we clearly observed three peaks representing three branches of spin-wave excitations, as shown in the middle and bottom panels of Fig. 3(a), respectively. Figure 3(b) shows constant-energy scans taken along two independent high-symmetry directions from the Γ-point to the M- and K-points [Fig. 4(c)]. For both constant-$\boldsymbol{Q}$ and constant-energy scans, the peak width is resolution-limited and the line shape is well described by the convolution with the resolution function. As the temperature increases toward T_N, the energy of the spin gap Δ, which scales with the order parameter, decreases toward zero and the peak width Γ, which is resolution-limited below 7 K, becomes broader, indicative of the shorter lifetime of the excitations, as shown in the inset

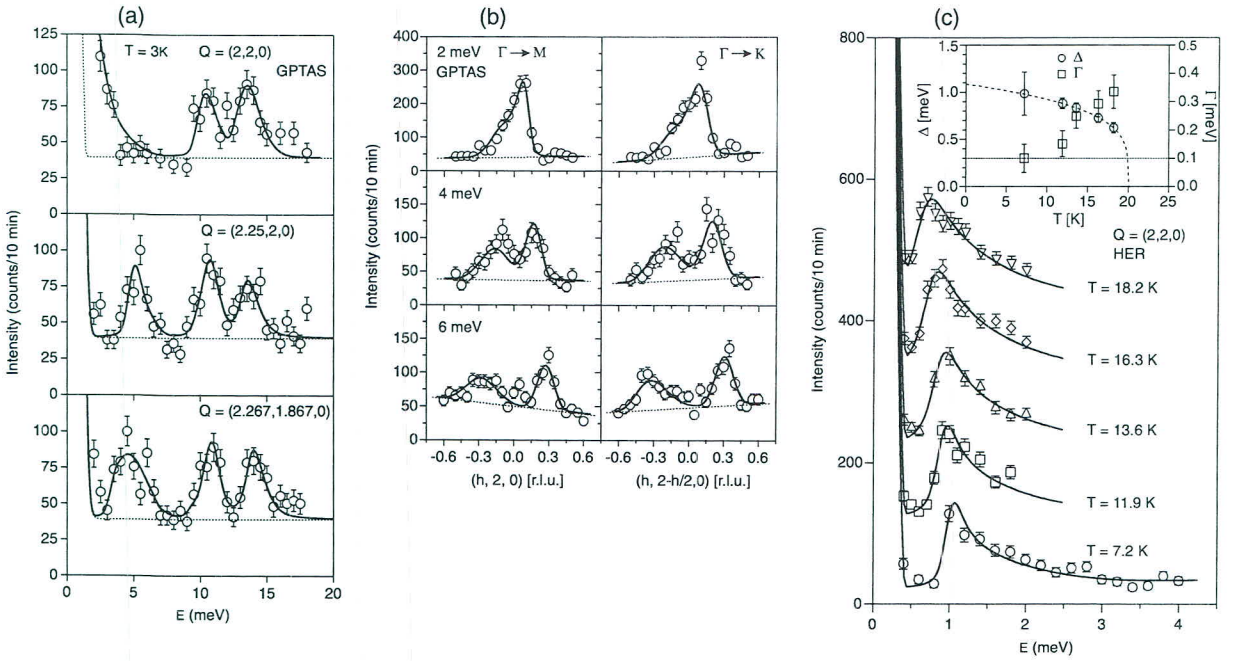

Fig. 3. (a) Constant-$\boldsymbol{Q}$ scans measured at $\boldsymbol{Q} = (2, 2, 0)$, $(2.25, 2, 0)$, and $(2.267, 1.867, 0)$. (b) Constant-energy scans measured at $\hbar\omega = 2$, 4, and 6 meV along two independent high-symmetry directions [see Fig. 4(c)]. (c) Temperature dependence of the spin gap at the Γ-point. The main panel shows constant-$\boldsymbol{Q}$ scans measured at the Γ-point at different temperatures. Data sets for different temperature are shifted vertically by 100. The inset shows the temperature dependences of the spin-gap energy Δ and peak width Γ. The dotted line denotes the resolution of the instrument obtained by the convolution fitting, and the dashed lines serve as a visual guide. The error bar denotes the statistical error.

of Fig. 3(c). Figures 4(a) and 4(b) show the spin-wave dispersions obtained from several constant-energy and constant-$\boldsymbol{Q}$ scans throughout the Brillouin zone along the two high-symmetry directions. The data points were obtained from resolution-convolution fits. Unfortunately, we were not able to determine the excitation energies of the high-energy modes owing to the high phonon background and low scattering intensity, which may be due to magnon instability.[28)]

We analyze the low-energy spin-wave dispersion observed in $Cs_2Cu_3SnF_{12}$ in the framework of LSWT. The underlying spin structure used to calculate the spin-wave dispersion is that of the $\boldsymbol{q} = 0$ structure for the uniform kagome lattice, in which all spins are oriented either toward or away from the center of a triangle [see Fig. 1(b)]. In our previous study on $Rb_2Cu_3SnF_{12}$ (Ref. 22), we found that the DM interactions play a dominant role in singlet–triplet excitations, i.e., a large out-of-plane component of the DM vectors gives rise to large splitting between the $S^z = \pm 1$ and 0 modes and reduces the energy gap at the Γ-point. Therefore, as a first approximation, we consider the DM interactions as the dominant anisotropy energy (referred to as the DM model), and express the spin Hamiltonian as

$$\mathcal{H} = \sum_{\langle i,j \rangle} \{J_{ij}(\boldsymbol{S}_i \cdot \boldsymbol{S}_j) + \boldsymbol{D}_{ij} \cdot [\boldsymbol{S}_i \times \boldsymbol{S}_j]\} + J_2 \sum_{\langle\langle k,l \rangle\rangle} (\boldsymbol{S}_k \cdot \boldsymbol{S}_l), \quad (1)$$

where J_{ij} and J_2 are the nearest-neighbor (NN) and next-nearest-neighbor (NNN) exchange interactions, respectively, and $\boldsymbol{D}_{ij}$ are DM vectors. J_{ij} are nonuniform as shown in Fig. 1(b), and their magnitude is scaled by J_1, which can be written as $J_{1i} = a_i J_1$ where $i = 1$, 2, 3, and 4, while the strength of the DM vectors $\boldsymbol{D}_{ij}$ is scaled by the corresponding exchange interactions, $D^{\parallel}_{ij} = d_z J_{ij}$ and $D^{\perp}_{ij} = d_p J_{ij}$, where the configurations of the out-of-plane ($D^{\parallel}_{ij}$) and in-plane ($D^{\perp}_{ij}$) components of the DM vectors are illustrated in Fig. 1(b). We neglect the interlayer interaction, because the triplet excitations in $Rb_2Cu_3SnF_{12}$ are dispersionless perpendicular to the kagome layer.[22)]

The LSWT calculations of the spin-wave dispersion as well as the scattering intensity for the DM model of Eq. (1), which are shown in Fig. 4(c) and Fig. S2 in Supplemental Materials,[29)] were performed using a symbolic algebra method written in Mathematica. Details of the LSWT calculations are described in Supplemental Materials.[29)] The results reveal 12 branches of spin-wave excitations, but only three dominant low-energy branches (Fig. S2) are observed experimentally. The strong inelastic scattering intensity centered around $\boldsymbol{Q}_m$ [Fig. 4(c)] is consistent with the experimental data. The obtained fit parameters are $J_1 = 13.6(3)$ meV, $a_1 = 1$ (fixed), $a_2 = 1.0(1)$, $a_3 = 0.84(7)$, $a_4 = 0.70(5)$, $J_2 = -1.07(2)$ meV, $d_z = -0.29(1)$ and $d_p = 0.057(4)$, giving $J^{sw}_{avg} = (J_{11} + J_{12} + J_{13} + J_{14})/4 = 12.1(7)$ meV. The solid lines in Figs. 4(a) and 4(b) represent the best fits with these parameters. The splitting of the two higher energy modes [ω_1 and ω_2, see Figs. 4(a) and 4(b)] at the Γ-point results from zone folding due to the structural transition. In the DM model, the energies of the ω_1 and ω_2 modes at the Γ-point are mainly determined by the out-of-plane component $D^{\parallel}$ of the DM vectors and the exchange interactions. The value of $D^{\parallel}$ is as large as $0.29J_{1i}$, which is the same order of magnitude as the value of $D^{\parallel}$ observed in $Rb_2Cu_3SnF_{12}$ (Ref. 22). This large out-of-plane component

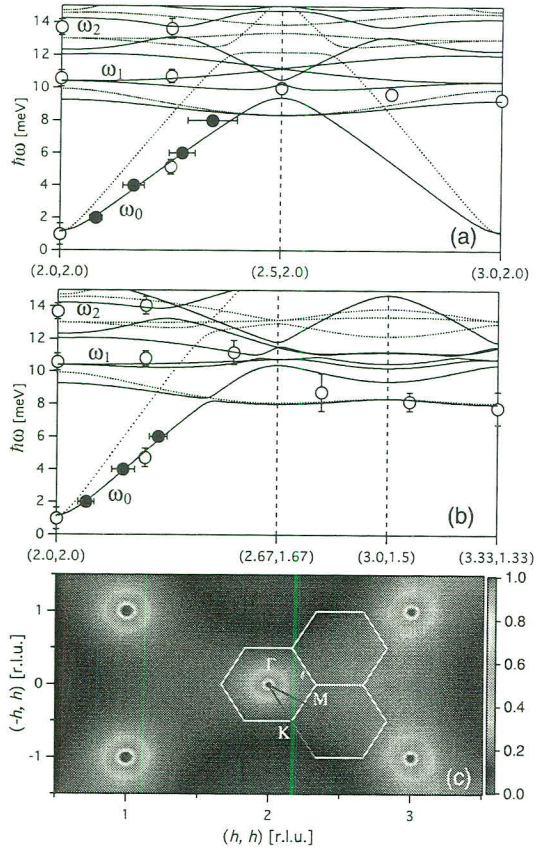

Fig. 4. (Color online) (a, b) Experimental data and calculated spin-wave dispersions along the two high-symmetry directions denoted by thick red lines in (c). Open symbols indicate the data measured around $(2,2,0)$ while closed symbols indicate the data measured at the equivalent point around $(0,2,0)$. Solid lines denote the best fit obtained using the DM model in Eq. (1), and dotted lines denote dispersions with $J_{\rm avg}^{\rm mag} = 19.8$ meV obtained from the magnetic susceptibility, $J_2 = -1.07$ meV, $d_z = -0.18$, and $d_{\rm p} = 0.033$. (c) Calculated energy-integrated scattering intensity of $Cs_2Cu_2SnF_{12}$.

of the DM vectors stabilizes the $\boldsymbol{q} = 0$ state, and thus is responsible for the magnetic ordering in $Cs_2Cu_3SnF_{12}$ as discussed by Cépas et al.[30] For a uniform kagome lattice, the in-plane component $D^{\perp}$ gives rise to the splitting of the ω_1 and ω_2 modes and the spin gap Δ, which are expressed as $\omega_2 - \omega_1 = (2D^{\perp}D^{\parallel})/(J_1 + J_2)$ and $\Delta = \sqrt{3}D^{\perp}$, respectively. The large splitting of the ω_1 and ω_2 modes and the small spin gap Δ cannot be consistently described by the DM model with uniform J_1, attesting to the necessity of a spin model with the enlarged unit cell and nonuniform J_{1i}. The ω_1 branch, which corresponds to the zero-energy mode in the absence of the DM interactions, is lifted considerably owing to the large $D^{\parallel}$. Its weak dispersion and lowest spin gap at the K-point can be ascribed to a small ferromagnetic next-nearest-neighbor interaction ($J_2 < 0$). Another possibility accounting for the dispersion of the ω_1 mode is the quantum fluctuations, which are dominant for the spin-1/2 case and favor the $\sqrt{3} \times \sqrt{3}$ ordering at the K-point over the $\boldsymbol{q} = 0$ ordering.[3,22,24]

Although the spin-wave dispersion observed in $Cs_2Cu_3SnF_{12}$ is qualitatively understandable in terms of LSWT and the DM model, there is a large quantitative disagreement between the exchange constant $J_{\rm avg}$ obtained from the spin-wave dispersion ($J_{\rm avg}^{\rm sw} = 12.1$ meV) and that obtained from the magnetic susceptibility data $J_{\rm avg}^{\rm mag}$. As shown by the solid line in Fig. 2(a), the magnetic susceptibility is best described using $J_{\rm avg}^{\rm mag} = 19.8$ meV when the interaction coefficients a_i, J_2/J_1 and d_z are fixed, as those obtained from the spin-wave data with $d_{\rm p} = 0$. Here, we neglected the small in-plane component of the DM vector $d_{\rm p}$. $J_{\rm avg}^{\rm mag} = 19.8$ meV should be close to the true exchange constant. However, the dotted lines in Figs. 4(a) and 4(b), which represent LSWT with $J_{\rm avg}^{\rm mag}$, show a large discrepancy between the LSWT result and the data especially for the ω_0 mode. We note that the slope of this mode is predominantly determined by $J_{\rm avg}$. Therefore, we deduce that the quantum fluctuations decrease excitation energies from those obtained by LSWT, i.e., negative quantum renormalization of the excitation energies occurs in $Cs_2Cu_3SnF_{12}$. For a spin-1/2 triangular-lattice Heisenberg antiferromagnet, a recent theory predicts that at high energies spin-waves are strongly renormalized, so that the dispersion becomes flat.[28,31,32] However, in contrast to the case of the triangular lattice, the renormalization factor ($R = J_{\rm avg}^{\rm sw}/J_{\rm avg}^{\rm mag} = 0.61$) in $Cs_2Cu_3SnF_{12}$ appears to be independent of the momentum transfer.

We note the renormalization factors in other low-dimensional antiferromagnets. For $Cu(DCOO)_2{\cdot}4D_2O$, which is described as an $S = 1/2$ square-lattice antiferromagnet, the positive quantum renormalization with $R = 1.21$ was reported.[33] This renormalization factor coincides with theoretical result.[34,35] For Cs_2CuCl_4, in which antiferromagnetic chains are coupled to form a spatially anisotropic triangular-lattice antiferromagnet, a large renormalization factor of $R = 1.63$ was reported.[36] This large positive quantum renormalization is attributed not to the triangular geometry of the lattice but to the spinon excitations characteristic of antiferromagnetic chain.[37] For $KFe_3(OH)_6(SO_4)_2$, which is described as an $S = 5/2$ uniform KLAF, the renormalization factor is estimated as $R = 0.90$ using the exchange constants determined from the dispersion relations[26] and magnetization and ESR measurements.[38] This fact together with the present result on $Cs_2Cu_3SnF_{12}$ shows that the negative quantum renormalization of the excitation energies is universal for KLAFs with an ordered ground state and enhanced with decreasing spin quantum number S.

Acknowledgments This work was supported by a Grant-in-Aid for Scientific Research from the Japan Society for the Promotion of Science, and the Global COE Program funded by the Ministry of Education, Culture, Sports, Science and Technology of Japan. H.T. was supported by a grant from the Mitsubishi Foundation. K.M. was supported by the Thailand Research Fund under grant No. MRG5580.

1) J. des Cloizeaux and J. J. Pearson, Phys. Rev. **128**, 2131 (1962).
2) Y. Endoh, G. Shirane, R. Birgeneau, P. Richards, and S. Holt, Phys. Rev. Lett. **32**, 170 (1974).
3) S. Sachdev, Phys. Rev. B **45**, 12377 (1992).
4) C. Waldtmann, H.-U. Everts, B. Bernu, C. Lhuillier, P. Sindzingre, P. Lecheminant, and L. Pierre, Eur. Phys. J. B **2**, 501 (1998).
5) H. Nakano and T. Sakai, J. Phys. Soc. Jpn. **80**, 053704 (2011).
6) F. Wang and A. Vishwanath, Phys. Rev. B **74**, 174423 (2006).
7) M. Hermele, Y. Ran, P. A. Lee, and X.-G. Wen, Phys. Rev. B **77**, 224413 (2008).
8) S. Yan, D. A. Huse, and S. R. White, Science **332**, 1173 (2011).
9) S. Depenbrock, I. P. McCulloch, and U. Schollwöck, Phys. Rev. Lett. **109**, 067201 (2012).
10) S. Nishimoto, N. Shibata, and C. Hotta, Nat. Commun. **4**, 2287 (2013).

11) R. R. P. Singh and D. A. Huse, Phys. Rev. B **77**, 144415 (2008).
12) G. Evenbly and G. Vidal, Phys. Rev. Lett. **104**, 187203 (2010).
13) K. Hwang, Y. B. Kim, J. Yu, and K. Park, Phys. Rev. B **84**, 205133 (2011).
14) M. P. Shores, E. A. Nytko, B. M. Bartlett, and D. G. Nocera, J. Am. Chem. Soc. **127**, 13462 (2005).
15) J. S. Helton, K. Matan, M. P. Shores, E. A. Nytko, B. M. Bartlett, Y. Yoshida, Y. Takano, A. Suslov, Y. Qiu, J.-H. Chung, D. G. Nocera, and Y. S. Lee, Phys. Rev. Lett. **98**, 107204 (2007).
16) T.-H. Han, J. S. Helton, S. Chu, D. G. Nocera, J. A. Rodriguez-Rivera, C. Broholm, and Y. S. Lee, Nature **492**, 406 (2012).
17) M. Müller and B. G. Müller, Z. Anorg. Allg. Chem. **621**, 993 (1995).
18) Z. Hiroi, M. Hanawa, N. Kobayashi, M. Nohara, H. Takagi, Y. Kato, and M. Takigawa, J. Phys. Soc. Jpn. **70**, 3377 (2001).
19) Y. Okamoto, H. Yoshida, and Z. Hiroi, J. Phys. Soc. Jpn. **78**, 033701 (2009).
20) T. Ono, K. Morita, M. Yano, H. Tanaka, K. Fujii, H. Uekusa, Y. Narumi, and K. Kindo, Phys. Rev. B **79**, 174407 (2009).
21) K. Morita, M. Yano, T. Ono, H. Tanaka, K. Fujii, H. Uekusa, Y. Narumi, and K. Kindo, J. Phys. Soc. Jpn. **77**, 043707 (2008).
22) K. Matan, T. Ono, Y. Fukumoto, T. J. Sato, J. Yamaura, M. Yano, K. Morita, and H. Tanaka, Nat. Phys. **6**, 865 (2010).
23) K. Matan, Y. Nambu, Y. Zhao, T. J. Sato, Y. Fukumoto, T. Ono, H. Tanaka, C. Broholm, A. Podlesnyak, and G. Ehlers, Phys. Rev. B **89**, 024414 (2014).
24) K. Hwang, K. Park, and Y. B. Kim, Phys. Rev. B **86**, 214407 (2012).
25) G. Misguich and P. Sindzingre, Eur. Phys. J. B **59**, 305 (2007).
26) K. Matan, D. Grohol, D. G. Nocera, T. Yildirim, A. B. Harris, S. H. Lee, S. E. Nagler, and Y. S. Lee, Phys. Rev. Lett. **96**, 247201 (2006).
27) T. Yildirim and A. B. Harris, Phys. Rev. B **73**, 214446 (2006).
28) A. L. Chernyshev and M. E. Zhitomirsky, Phys. Rev. B **79**, 144416 (2009).
29) (Supplemental Material) Details of the LSWT calculations of the spin-wave dispersion and the scattering intensity for the DM model of Eq. (1) are described in Supplemental Materials.
30) O. Cépas, C. M. Fong, P. W. Leung, and C. Lhuillier, Phys. Rev. B **78**, 140405(R) (2008).
31) O. A. Starykh, A. V. Chubukov, and A. G. Abanov, Phys. Rev. B **74**, 180403(R) (2006).
32) W. Zheng, J. O. Fjærestad, R. R. P. Singh, R. H. McKenzie, and R. Coldea, Phys. Rev. B **74**, 224420 (2006).
33) H. M. Rønnow, D. F. McMorrow, R. Coldea, A. Harrison, I. D. Youngson, T. G. Perring, G. Aeppli, O. Syljuåsen, K. Lefmann, and C. Rischel, Phys. Rev. Lett. **87**, 037202 (2001).
34) J. Igarashi, Phys. Rev. B **46**, 10763 (1992).
35) R. R. P. Singh and M. P. Gelfand, Phys. Rev. B **52**, R15695 (1995).
36) R. Coldea, D. A. Tennant, and Z. Tylczynski, Phys. Rev. B **68**, 134424 (2003).
37) M. Kohno, O. A. Starykh, and L. Balents, Nat. Phys. **3**, 790 (2007).
38) T. Fujita, H. Yamaguchi, S. Kimura, T. Kashiwagi, M. Hagiwara, K. Matan, D. Grohol, D. G. Nocera, and Y. S. Lee, Phys. Rev. B **85**, 094409 (2012).